# A new phantom to assess and correct geometrical distortions for Magnetic Resonance Imaging: Design and preliminary experiments

Maximilien Vermandel, Nacim Betrouni

# A new phantom to assess and correct geometrical distortions for Magnetic Resonance Imaging: design and preliminary experiments

M. Vermandel[1,2,3], N. Betrouni[3]
1- University hospital of Lille – CHRU, Lille F-59000, France
2 – Université de Lille , Lille, F59000, France
3 – Inserm, U1189 – ONCO-THAI, Lille, F59000, France

**Abstract**:

**Purpose:**
Nowadays, many focal therapies use Magnetic Resonance imaging (MR) for treatment planning purpose. In this context, geometric distortions should be as low as possible. In this paper, we present a new device to assess image distortions in MRI.
**Methods:**
The phantom consists in a stack of plates made of Polymethyl Methacrylate (PMMA). The detection elements are balls forming MRI capsules and delimiting an internal volume filled with paraffin oil. When imaged, this system enables having a regular pattern with the same distance in the 3 space directions between each capsule center of mass.
Correction of the distortions is done using a registration of the detected balls pattern with the theoretical pattern. Iterative Closest Points (ICP) algorithm is used for thus purpose.
**Results:**
Preliminary evaluations on different MR sequences have been conducted, the combination of device and ICP-based correction method show the feasibility of the approach.
**Conclusion:**
From the promising preliminary results obtained, future developments will include an upgrade of the phantom and the implementation of more sophisticated correction algorithms.

**Keywords**: Geometrical distortions, MRI, Quality assessment, phantom, image guided therapy

## 1. Introduction:

Focal therapy refers to a variety of minimally invasive techniques such as High Intensity Focused Ultrasound (HIFU), LASER, cryotherapy, radiosurgery or hypo-fractionated radiotherapy for destroying tumors while sparing normal surrounding tissue. This technique is generally performed under image guidance, and necessitates going through a preliminary treatment planning stage to obtain an accurate delineation of tumor volume and adjacent structures at risk. Among the possible imaging modalities, Magnetic Resonance Imaging (MRI) offers a good soft tissue contrast but may suffer in counterpart from geometric distortions that mainly come from gradient field non-

linearity and magnet field inhomogeneity. These distortions appear under the form of pixel shift and intensity variation in the image volume.

In MRI, several issues may induce these distortions (1, 2) (3). These sources of distortions can be analyzed from intrinsic and extrinsic points of view. The main cause of intrinsic distortions is the heterogeneity of the main field $B_0$. Distortions due to this phenomenon are proportional to $B_0$ (4) leading to MRI spatial encoding distortions increasing with higher magnetic field strength (5), almost near the external limits of the field of view (FOV). Nonlinear gradient is also an intrinsic source of distortions. Nonlinear gradient distortions affect precision and accuracy and are typical of the latest generation of MR scanner (6). The build of new MRI scanner with higher magnetic fields, shorter bores, higher gradients and shorter gradient rise times mainly causes these nonlinear gradient distortions. « Barrel-shaped » distortions on morphometric images are specific of such nonlinear gradients (7-10). Extrinsic distortions are mainly due to the patient himself (difference of magnetic susceptibility, prosthesis, implants, surgical clips...), hardware set-up on the patient (e.g. stereotactic frame) and chemical shift.

Distortion correction has been the subject of a certain number of works. They can be classified into two families: online and offline techniques. The first one is applied during the image reconstruction process and is based on the magnetic field maps while the second one makes use of designed phantoms to estimate these distortions and then apply a correction technique on the image volume. Our work has focused on the latter one.

In this paper, preliminary results obtained from a new device and from application of basics correction processing (9) are described in the following sections.

## 2. Related works

### a. Correction methods

#### i. Correction from magnetic fields map

Magnetic field maps describe the spatial magnetic field heterogeneity on images. A map can be estimated from the phase of a complex image. Measuring the phase variations (i.e. the magnetic field) from multiple echoes, spaced in time inside a given MRI sequence, enables to create a voxel shifts map. This map is thereafter used to correct the distortions.

This approach was used in many studies (11-17). They were mainly focused on Echo planar Imaging (EPI) technics and applied for functional MRI (fMRI).

### ii. Correction from phantom acquisitions

Correction of geometric distortions can also be applied offline from the space domain. Images acquired from phantom are post-processed in order to build-up distortion maps according to control points detected on the phantom images. This approach offers the advantage of correcting most of the field heterogeneities and gradient non-linearities (6, 7, 9, 18-23).

## b. Measurement and characterization of the MRI distortions

Different solutions were proposed to characterize MRI distortions from physical devices (phantoms). Doran *et al.* and Tanner *et al.* (21, 22) have proposed a Linearity Test Object (LTO) built from contrast agent filled rods suspended in the phantom. Another LTO consists in cylindrical bars placed in a tank filled with a contrast agent (eg. copper sulphate). The bars are thus observed as hypo-signal (Figure 1). A similar phantom is commercialized by Elekta (Elekta, Stockholm, Sweden) to check the MRI distortions for radiosurgery planning (24). Stereotactic frame can be set-up on this phantom to assess geometric distortions induced by the frame. Nevertheless, because of its configuration, it only enables to observe distortions in a single plan. Analyzing others plans requires changing the orientation of the LTO in the tank.

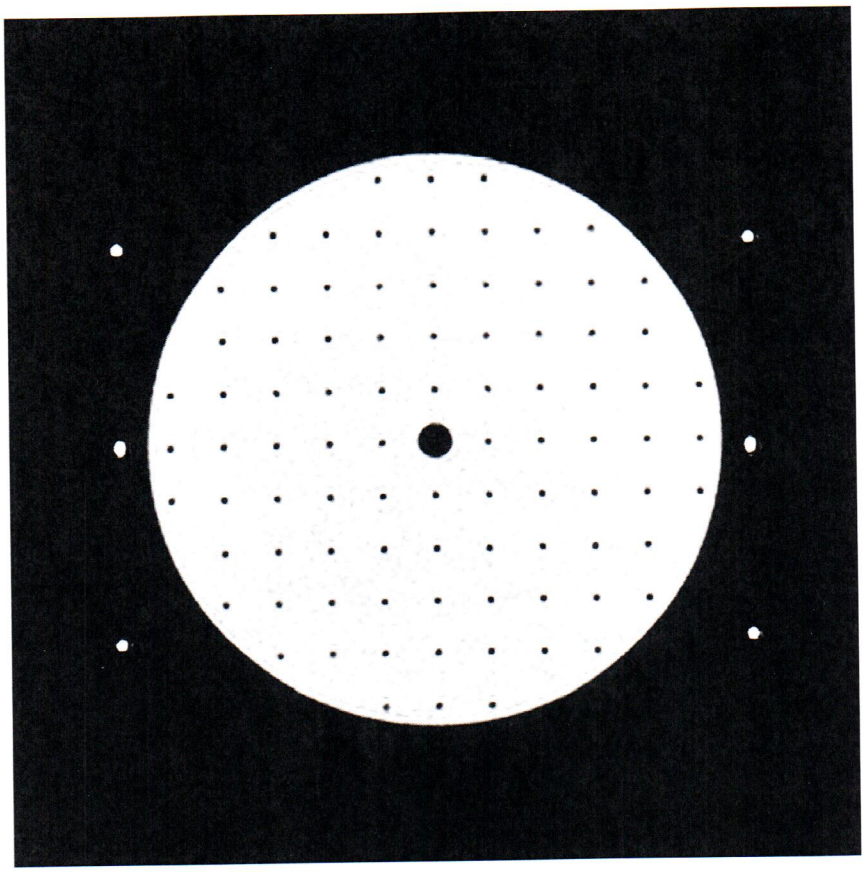

Figure 1: T1 weighted MR images with a phantom similar to the LTO but with plain bar

In the context of interventional MRI with open low-field magnet, Daanen *et al.* (20) have proposed a device able of characterizing large FOV. This calibration phantom consisted of 750 spherical glass balls (15 mm in diameter) arranged in a regular cubic pattern with 30-mm side length. The phantom dimensions were 400 x 210 x 300 $mm^3$ (patient coordinates: LR x AP x HF, spatial coordinates: horizontal (X) x vertical (Y) x horizontal (Z)), which corresponds to typical FOV sizes for abdomen examinations. Figure 2 shows images acquired in a large FOV configuration with this device. This device was also applied by Viard *et al.* (19) to characterize the distortions of a 0.2 T open magnet MRI. For instance, Figure 3 presents iso-values of the radial distortions before and after image correction. (The radial distortion is estimated from the theoretical position of the center of mass of a ball and its actual position measured on the images).

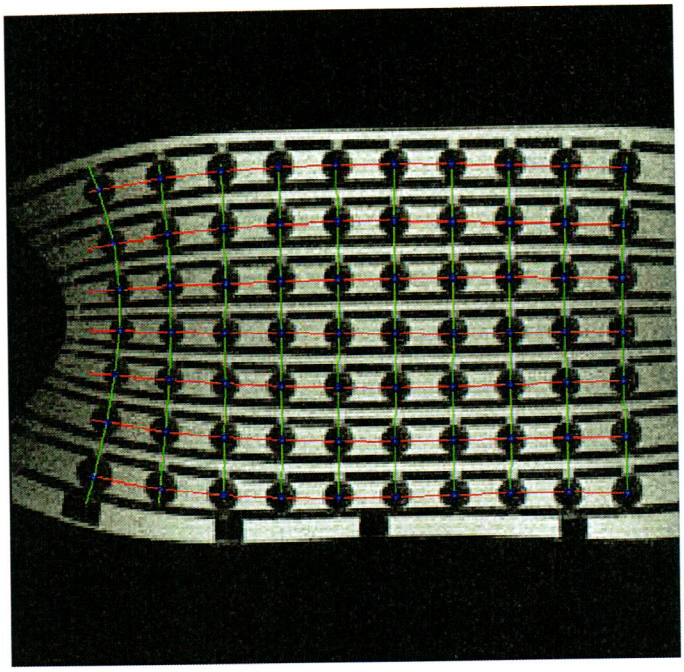

Figure 2: MR axial image and control points detection from the calibration phantom designed by Daanen et al. with a regular cubic pattern: 30 mm distance between each point. (images from (19), MR sequence: Fast Spin Echo – TR: 3500 ms – TE: 15 ms – Flip: angle 30° - FOV: 350 mm - Slice thickness: 5mm - 256x256 pixels).

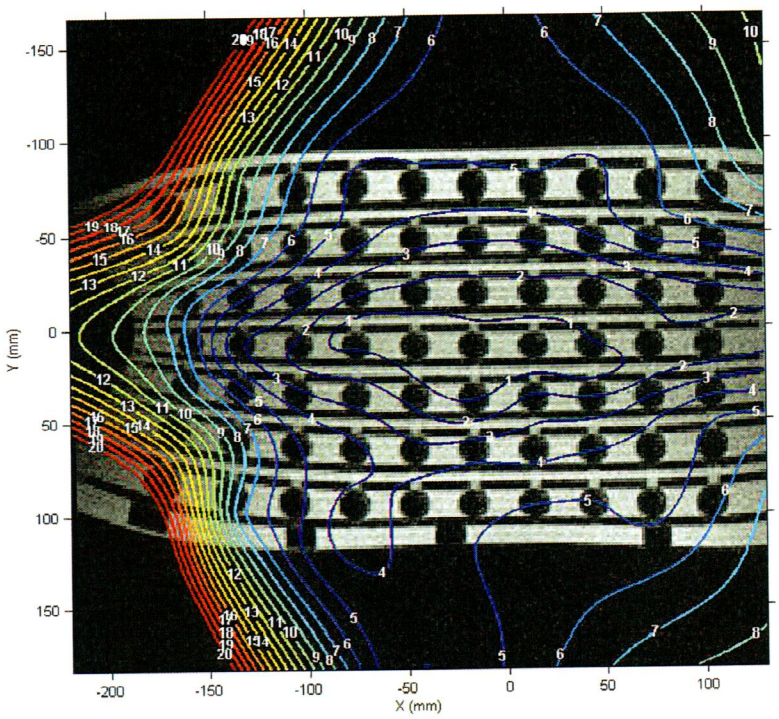


(a)

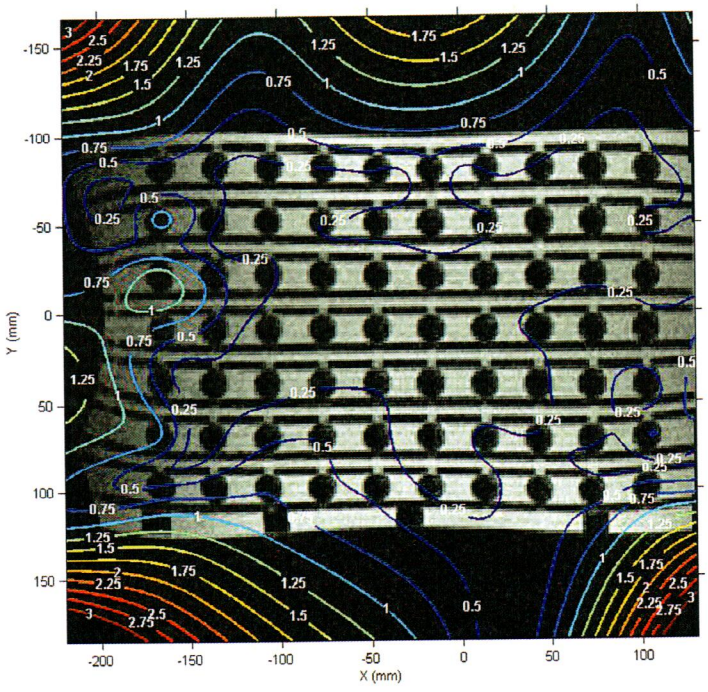


(b)

Figure 3: Distortions characterization, curves indicate the iso-value radial error in mm before (a) and after (b) correction (images from (19))

The control points from the two previous devices were observed as hyposignal. Wang and Doddrell (7, 8) proposed another device that allowed the use of control points in hypersignal. They described their phantom for a body coils as layers of parallel grid sheets aligned with equal spacing along the vertical direction to obtain a 3D array of points. The gap between the grids is equal to the grid thickness. Control points are deduced in 2D according to the intersection of the grid and the third dimensions is obtained according the interface between the contrast agent (copper sulfate) and the grid.

A similar phantom, used in (18, 25, 26), is now commercialized by Modus QA (Modus Medical Devices Inc. London, Canada) for brain MRI sequences in stereotactic condition (27). This phantom is built-up from an acrylic cube containing a 1 cm 3D grid of channels filled with copper sulfate solution. The main body of the phantom measures 14x13x11 $cm^3$ with 2002 control points.
This phantom offers the advantage of being easily build-up for different 3D arrays sizes according to the grid size and thickness. Nevertheless, the detection of control point is more difficult than the use of ball centers of mass.

In the next section we describe the design of a phantom allowing the acquisition of a 3D distortions map and an associated method to characterize and to correct them. Compare to latter devices described in the literature, the proposed device is able to characterize the distortions in any plan of space from any acquisition sequence, vertices are visible in hyper-signal and the assembly of the phantom is suitable to large or small FOV.

## 3. Material and Method

### a. Phantom specifications

The phantom consists of a stack of plates made of Polymethyl Methacrylate (PMMA). For each plate, the second surface is full whereas the first surface is pierced with an array of blind holes parallel to the central axis. The blind holes are arranged in rows and columns and are regularly spaced (figure 4 a). Detection elements are set-up in each hole. The detection elements are balls (5mm diameter) forming MRI capsules and comprise an envelope bearing a spherical surface and delimiting an internal volume filled with 0.032 ml of contrast agent. In our experiments, soft-gelatin capsule filled with paraffin oil were

used. This system enables to have a regular pattern with the same distance in the 3 space directions between each capsule center of mass (figure 4 b). The grid size or resolution pattern can easily be changed and the size of the phantom can be adapted according to the number of plates stacked or the diameter of each plates used. For the experiments, the prototype (figure 5) were built in such a manner that $d_x=d_y=d_z=1$cm in order to obtain a 3D grid of control points when considering the center of mass of each capsule.

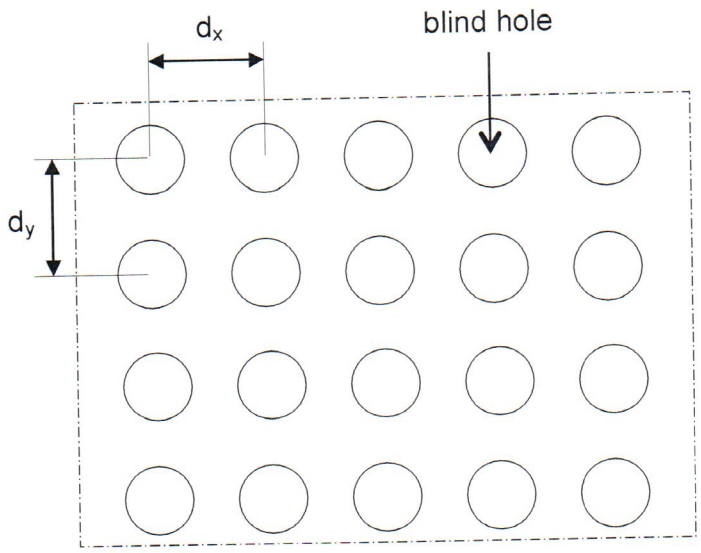


(a)

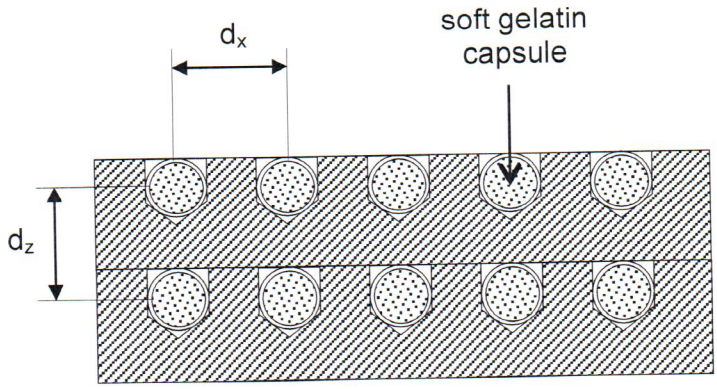


(b)

Figure 4: Design of the phantom. (a) Surface of a plate where holes are pierced to form a regular pattern ; (b) slice of two superimposed plates where the detection elements are set into the holes to have a 3D grid of control points according to distances $d_x$, $d_y$, $d_z$ when considering the center of mass of each capsule.

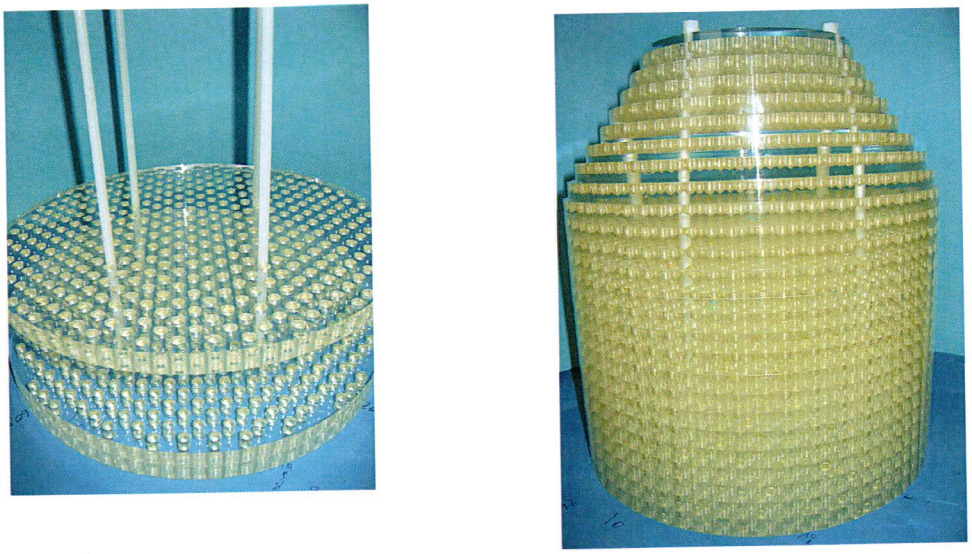

(a) (b)

Figure 5: Composition of the phantom (a) The assembly of the phantom ; (b) Phantom set-up in head coil configuration

### b. Characterization and correction of the distortions

Starting from phantom images acquired according to a specific MRI sequence, a set of different processes enable to characterize and to correct the distortions (figure 8).

i. Image post-processing

The center of mass of each capsule is estimated using a set of basic image processing tools (figure 6).

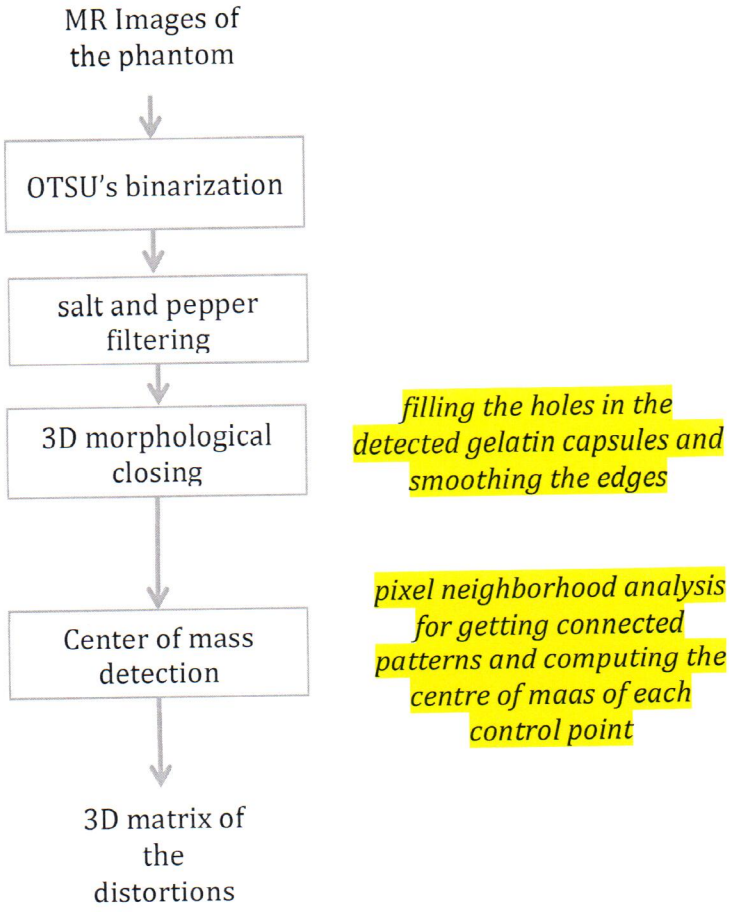


Figure 6: Pipeline of the post-processing steps leading to the distortions characterization.

ii. Evaluation of the distortions

Once control points extracted, corresponding to the center of mass of capsule, the Iterative Closest Point (ICP) (28) is applied to register them with the center of gravity position of the capsules on the physical phantom. In our experiments, the theoretical control points were arranged in a regular cubic pattern of 1cm side length. Finally, three-dimensional distortion map is generated by measuring the positional deviations at the control points:

$$
\begin{aligned}
dx_p &= x'_p - x_p \\
dy_p &= y'_p - y_p \\
dz_p &= z'_p - z_p \\
&or \\
dr_p &= \sqrt{(dx_p)^2 + (dy_p)^2 + (dz_p)^2} \\
&(p = 1,2...N)
\end{aligned}
\qquad \text{Eq. 1}
$$

where $x'_p$, $y'_p$ and $z'_p$ are the coordinates of the control point p measured in the distorted image space; $x_p$, $y_p$ and $z_p$ are the corresponding coordinates measured in the undistorted physical space of the phantom, and N is the total number of control points.

iii. Correction of the distortions

Once the 3D distortion map is known, the correction is achieved through an interpolation processing (7) based on equation 2:

$$
\begin{pmatrix} x' \\ y' \\ z' \end{pmatrix} = P \begin{pmatrix} x \\ y \\ z \end{pmatrix} \qquad \text{Eq. 2}
$$

where x, y, z are the coordinates of any given spatial point in the undistorted physical space; x', y', z' are the coordinates of its corresponding point in the distorted image space, and P represents an interpolation model through which this correspondence is established.

In order to manage local distortions, piecewise interpolation is used. First, a 3D cubic interpolation from the measured positional deviations at the control points (Eq. (1)) is computed: the values of distortion are thus given along the three axes of the space at each voxel of the volume to be corrected. In order to complete the correction process, a second interpolation is required for interpolating the voxel intensity: piecewise cubic interpolation is used and each voxel intensity of the corrected volume (re-sampled) is then assigned.

## 4. Experiments and Results

For the experiments, all the algorithms evaluated were implemented on an in-house software (ArtiMED - http://www.onco-thai.fr) developed on a Borland C++ platform, using OpenGL for visualization.).

Experiments have been achieved on different MRI sequences from two facilities (Table 1).

Table 1: the different sequences and facilities evaluated

| | MRI System | Sequence | TE (ms) | TR (ms) | Matrix size | Number of slices | Voxel size ($mm^3$) |
|---|---|---|---|---|---|---|---|
| **I** | Philips Achieva 1.5 T | MRA-DSA (dynamic angiography) | 1.336 | 4.245 | 256x256 | 240 | 1x1x1 |
| **II** | Philips Achieva 3 T | BFFE | 2.37 | 6.118 | 576x576 | 80 | 0.43x0.43x1 |
| **III** | Philips Achieva 3 T | 3D NeuroNav SENSE T1 | 1.868 | 20 | 256x256 | 250 | 1x1x1 |
| **IV** | Philips Achieva 1.5 T | 3D Nav T1 (st1_3d_ffe1mm) | 4.597 | 25 | 256x256 | 180 | 0.9x0.9x1 |

Accuracy was assessed by estimating the measured residual geometric distortions in the corrected images. If the positions of the control points have been measured accurately, the corrected images can then be expected to contain little or no geometric distortion. Any residual distortion measured in the corrected images can then be used as an overall measure of the accuracy. This method has also been used by previous investigators (7, 18).

Figure 7 illustrates the correction on several slices of an MR examination where it can be observed that the "potatoes chips" effect is partially corrected from piecewise interpolation.

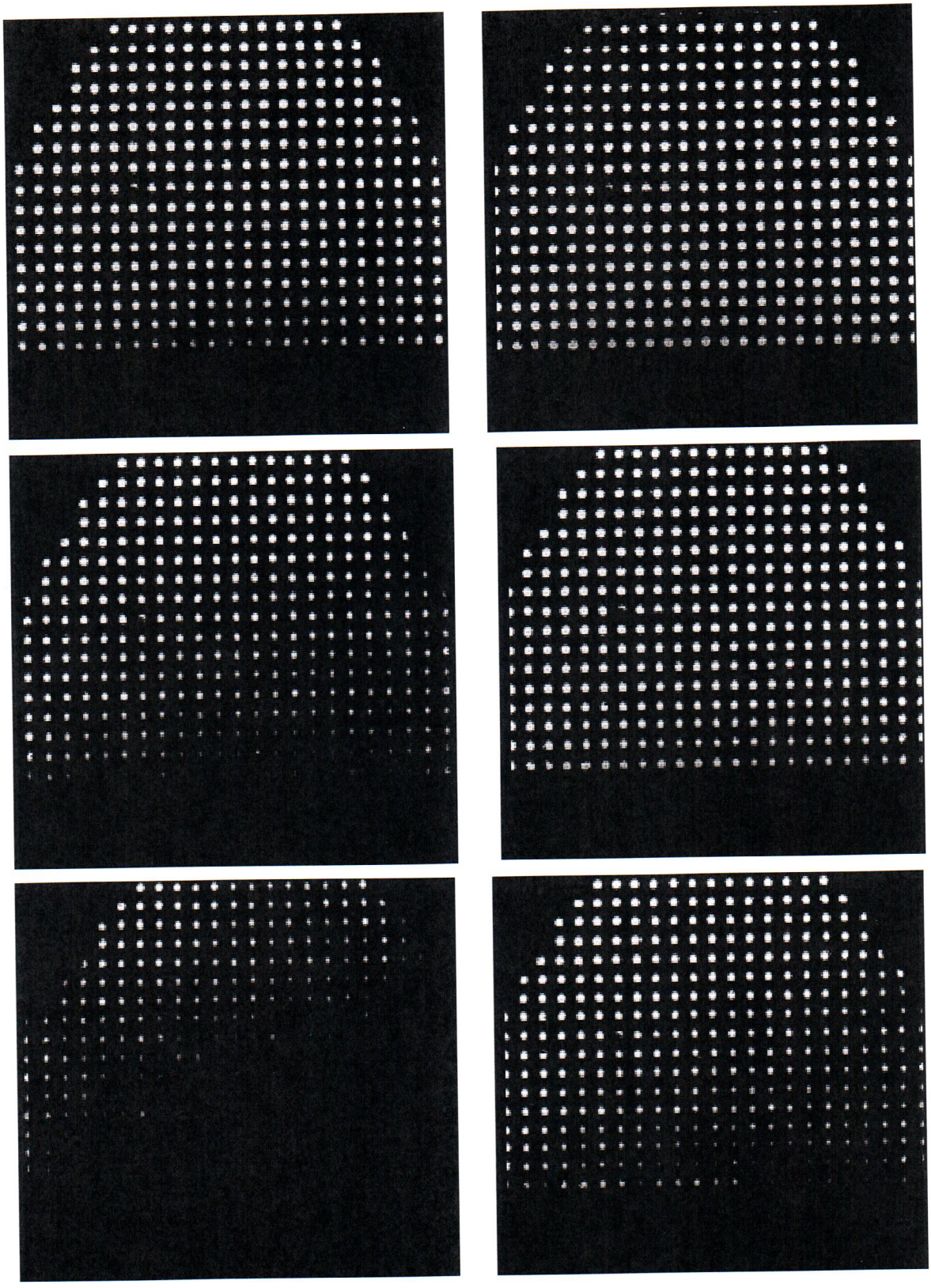

(a) (b)

Figure 7: Example of correction on four successive sagittal slices of a T1 MRI sequence (row IV in table 1), (a) uncorrected images, (b) corrected images. The slices are located on both sides of the isocenter

For each sequence, mean and standard deviation were reported before and after correction. The values are summarized in table 2.

Table 2: Detected and corrected distortions for each MR sequence.

| | **Mean (mm)** | | **Standard-Deviation (mm)** | | **Maximum (mm)** | |
|---|---|---|---|---|---|---|
| | Uncorrected image | Corrected image | Uncorrected image | Corrected image | Uncorrected image | Corrected image |
| **I** | 1.03 | 0.51 | 0.61 | 0.21 | 3.36 | 2.37 |
| **II** | 0.24 | 0.22 | 0.11 | 0.09 | 0.92 | 0.82 |
| **III** | 0.37 | 0.34 | 0.17 | 0.17 | 2.2 | 2.19 |
| **IV** | 0.44 | 0.34 | 0.27 | 0.15 | 2.36 | 1.55 |

As the distortions were low for some sequences, the mean and standard deviation were not always appropriate to estimate the residual distortions. To highlight the correction effect, we plot the frequency of apparition of distortion levels through a histogram representation (eg. number of a given 3D error observed in the entire volume). This representation depicts the correction through a shift to the left of the frequency. The figure 8 shows the different histograms.

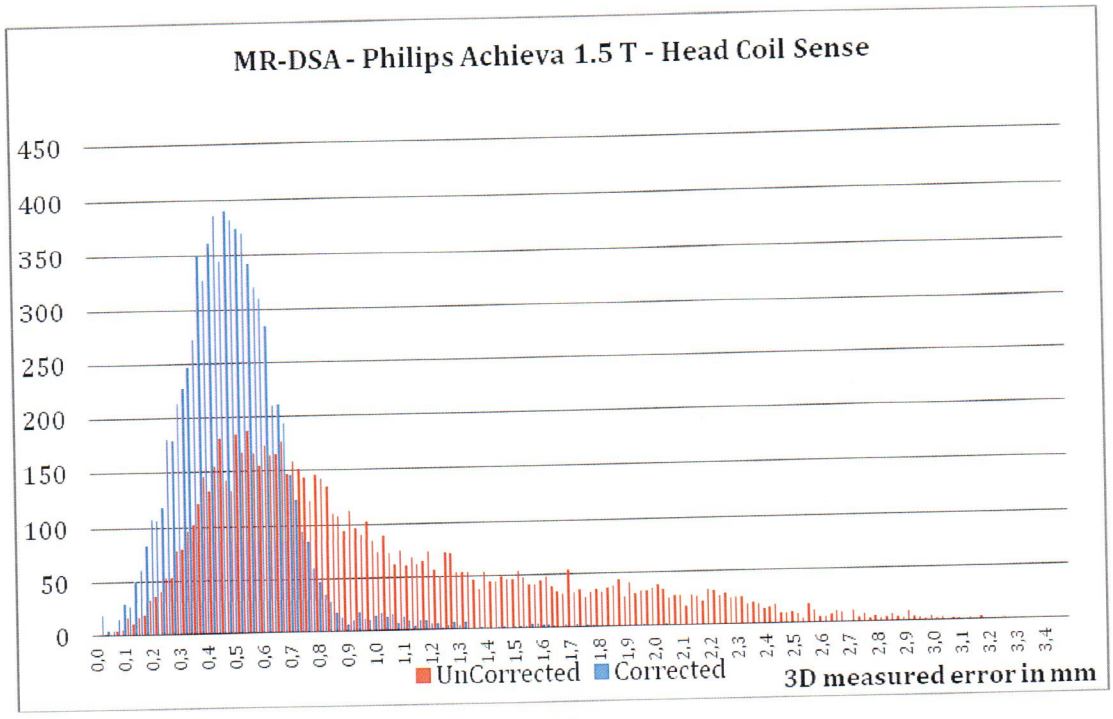
MR-DSA - Philips Achieva 1.5 T - Head Coil Sense
450
400
350
300
250
200
150
100
50
0
0,0 0,1 0,2 0,3 0,4 0,5 0,6 0,7 0,8 0,9 1,0 1,1 1,2 1,3 1,4 1,5 1,6 1,7 1,8 1,9 2,0 2,1 2,2 2,3 2,4 2,5 2,6 2,7 2,8 2,9 3,0 3,1 3,2 3,3 3,4
UnCorrected
Corrected
3D measured error in mm

(a)

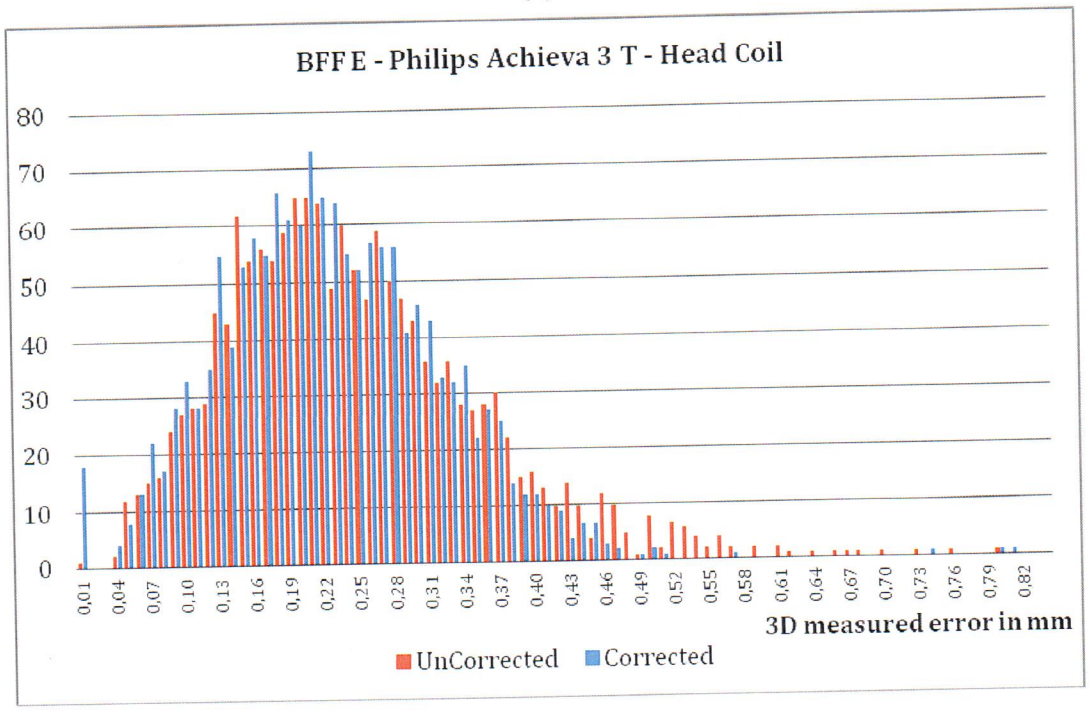
BFF E - Philips Achieva 3 T - Head Coil
80
70
60
50
40
30
20
10
0
0,01 0,04 0,07 0,10 0,13 0,16 0,19 0,22 0,25 0,28 0,31 0,34 0,37 0,40 0,43 0,46 0,49 0,52 0,55 0,58 0,61 0,64 0,67 0,70 0,73 0,76 0,79 0,82
3D measured error in mm
UnCorrected
Corrected

(b)

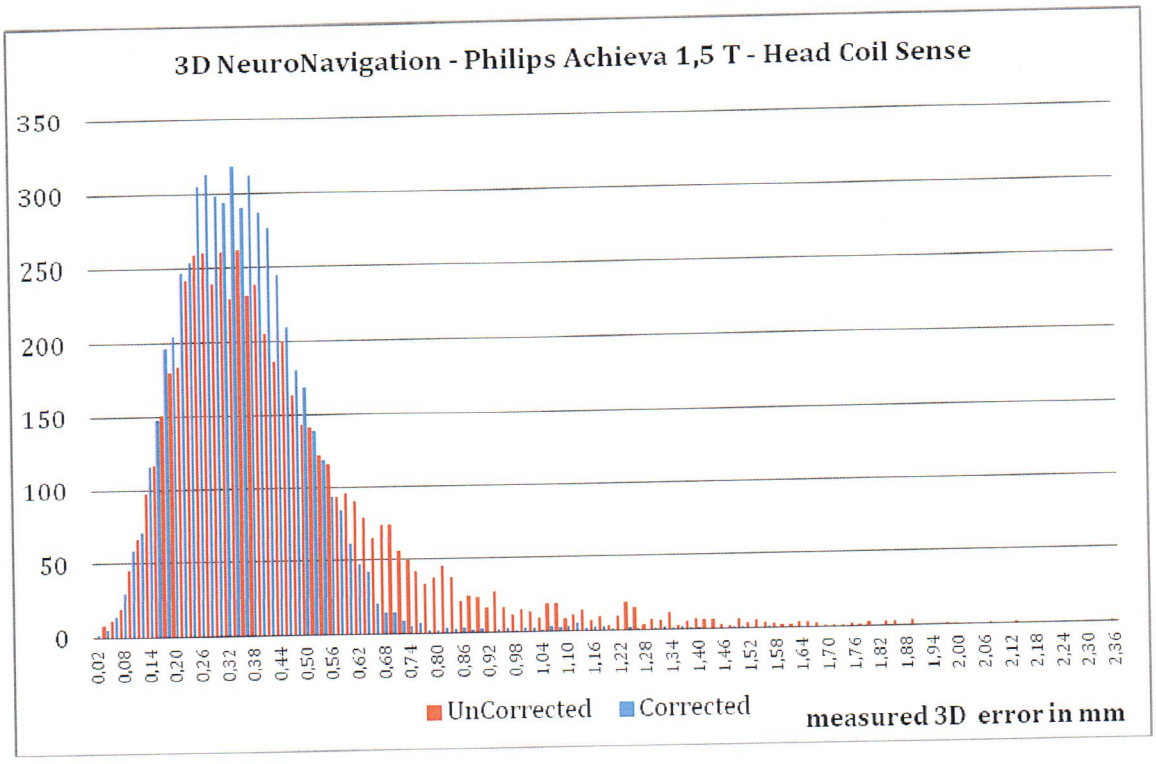


(c)

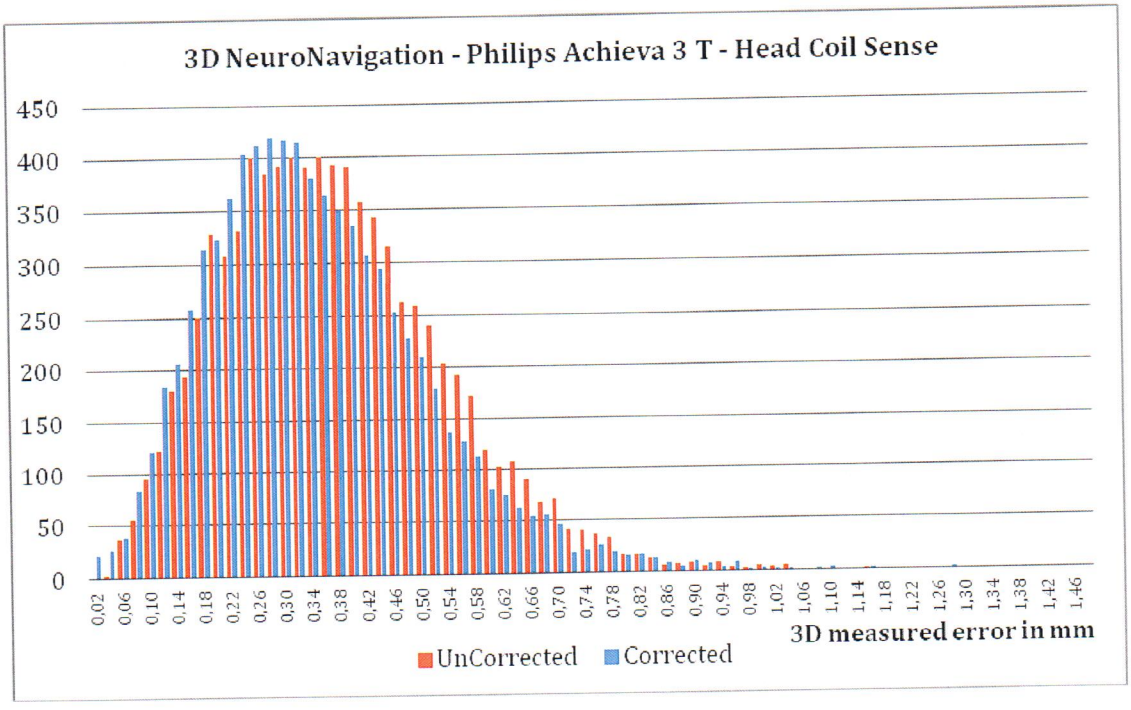


(d)

Figure 8: Histograms of the distortions encountered before and after correction for the different MR sequences (a) MR-DSA 1.5 T, (b) BFFE 3 T, (c) 3D T1 – 3T, (d) 3D T1 1.5 T.

Visual assessment of the distortions and the applied corrections are additional control features of the software platform (figure 9).

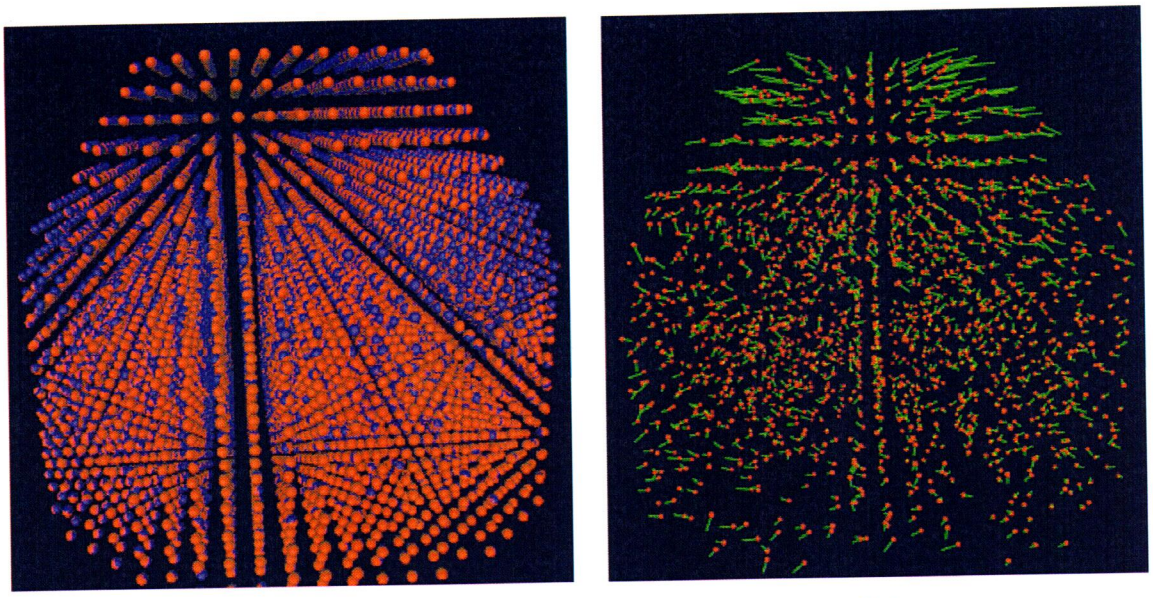

(a) (b)

Figure 9: Image of the phantom after image post-processing, in (a) theoretical control points are shown in blue and the control points measured on the phantom are shown in red, (b) show the map of the distortion field through vector representation.

## 5. Discussion

The distortions observed in MR imaging are tolerated for diagnostic purpose but still have to be addressed for MR guided therapies. In this context, we have proposed a new phantom able of measuring accurately the distortions and, by the mean of correction algorithms, to reduce the distortions. We have reported in this paper the feasibility and the preliminary results.

Many of its features make it particularly interesting with respect to others available phantoms. First of all, the phantom was designed without the requirement of contrast agent (copper sulphate, gadolinium...). This feature makes it very user-friendly since it does not require to be filled or re-filled and thus avoid removing of air bubbles when specially complex shapes or tiny structures are used (7, 22, 23). Furthermore, the plates design makes the shape of the phantom fully suitable for complete 3D analysis using

different coils (body, head...) since the number of plates can be easily adjusted. Thus, a single device with a set of different sized plates might fit multiple FOV. The image post-processing and the detection of the centers of mass can be achieved easily thanks to the use of soft-gelatin capsule. The 3D vertices used for distortions evaluation and correction are thus obtained in an easier manner than the 3 plans method proposed by Wang *et al* (7) for example. The simplification of the post-processing step should lead to a more accurate location of the control points. Another interesting aspect of the phantom is that the vertices are visualized through hyper-signal.

In the results section, preliminary results tend to show that a simple correction algorithm could lead to an acceptable minimization of the distortions. The observation of the histograms (figure 9) demonstrates the effect of the correction even when handling very low distortions.

In this study, the use of an ICP algorithm and piecewise interpolation was a preliminary implementation to simply evaluate the ability of the phantom to provide accurate measurement. We are aware that a more robust registration algorithm should be used. In particular, when considering that the ICP implementation manages only rigid transformation for the theoretical / measured control points pairing. A non-rigid algorithm will be experienced with a larger dataset including clinical images and digitally simulated images with known levels of distortions. Furthermore, a more complete experimental design will be set-up to evaluate how this new device outperforms existing phantom.

## 6. Conclusion

In this paper, we have described preliminary results of a new phantom to evaluate and correct image distortions that occurs in MRI. Thanks to an original design (ie. a of stack of plates, no contrast agent), this phantom may fit any field of view. Indeed, the phantom can easily be assembled with different plates of different size.

Future developments will be focused on the adaptability to stereotactic imaging. Thus, the phantom will be upgraded to support stereotactic frame, specially the Leksell frame (from Elekta) widely used for stereotactic neurosurgery. This evolution is necessary since the main source of uncertainty for stereotactic MRI is the presence of the frame during the image acquisition.

This new design combined with a more efficient algorithm will be applied to evaluate the feasibility of using 3T MRI facilities for stereotactic imaging.


## ACKNOWLEDGMENTS

The authors would like to thank M. Pascal Briche for his assistance in the assembly of the phantom prototype


## REFERENCES


1. Michiels J, Bosmans H, Pelgrims P, Vandermeulen D, Gybels J, Marchal G, et al. On the problem of geometric distortion in magnetic resonance images for stereotactic neurosurgery. Magn Reson Imaging. 1994;12(5):749-65.
2. Wang D, Doddrell DM. A proposed scheme for comprehensive characterization of the measured geometric distortion in magnetic resonance imaging using a three-dimensional phantom. Med Phys. 2004;31(8):2212-8.
3. Sewonu A, Hossu G, Felblinger J, Anxionnat R, Pasquier C. An automatic MRI quality control procedure: Multisite reports for slice thickness and geometric accuracy. IRBM. 2013;34(4–5):300-5.
4. Chang H, Fitzpatrick JM. A technique for accurate magnetic resonance imaging in the presence of field inhomogeneities. IEEE Trans Med Imaging. 1992;11(3):319-29.
5. Dammann P, Kraff O, Wrede KH, Ozkan N, Orzada S, Mueller OM, et al. Evaluation of hardware-related geometrical distortion in structural MRI at 7 tesla for image-guided applications in neurosurgery. Acad Radiol. 2011;18(7):910-6.
6. Caramanos Z, Fonov VS, Francis SJ, Narayanan S, Pike GB, Collins DL, et al. Gradient distortions in MRI: Characterizing and correcting for their effects on siena-generated measures of brain volume change. Neuroimage. 2010;49(2):1601-11.
7. Wang D, Doddrell DM, Cowin G. A novel phantom and method for comprehensive 3-dimensional measurement and correction of geometric distortion in magnetic resonance imaging. Magn Reson Imaging. 2004;22(4):529-42.
8. Wang D, Doddrell DM. Method for a detailed measurement of image intensity nonuniformity in magnetic resonance imaging. Med Phys. 2005;32(4):952-60.
9. Wang D, Strugnell W, Cowin G, Doddrell DM, Slaughter R. Geometric distortion in clinical MRI systems part ii: Correction using a 3d phantom. Magn Reson Imaging. 2004;22(9):1223-32.
10. Jovicich J, Czanner S, Greve D, Haley E, van der Kouwe A, Gollub R, et al. Reliability in multi-site structural MRI studies: Effects of gradient non-linearity correction on phantom and human data. Neuroimage. 2006;30(2):436-43.
11. Janke A, Zhao H, Cowin GJ, Galloway GJ, Doddrell DM. Use of spherical harmonic deconvolution methods to compensate for nonlinear gradient effects on MRI images. Magnetic resonance in medicine. 2004;52(1):115-22.
12. Eggers H, Knopp T, Potts D. Field inhomogeneity correction based on gridding reconstruction for magnetic resonance imaging. IEEE Trans Med Imaging. 2007;26(3):374-84.

13. Liu G, Ogawa S. Epi image reconstruction with correction of distortion and signal losses. J Magn Reson Imaging. 2006;24(3):683-9.
14. Chen NK, Wyrwicz AM. Optimized distortion correction technique for echo planar imaging. Magn Reson Med. 2001;45(3):525-8.
15. Chen NK, Oshio K, Panych LP. Application of k-space energy spectrum analysis to susceptibility field mapping and distortion correction in gradient-echo epi. Neuroimage. 2006;31(2):609-22.
16. Cusack R, Brett M, Osswald K. An evaluation of the use of magnetic field maps to undistort echo-planar images. Neuroimage. 2003;18(1):127-42.
17. Windischberger C, Robinson S, Rauscher A, Barth M, Moser E. Robust field map generation using a triple-echo acquisition. J Magn Reson Imaging. 2004;20(4):730-4.
18. Stanescu T, Jans HS, Wachowicz K, Fallone BG. Investigation of a 3d system distortion correction method for mr images. Journal of Applied Clinical Medical Physics. 2010;11(1).
19. Viard R, Mordon S, Betrouni N, Vermandel M, Vanhoutte M, Rousseau J. Correction of images in an open-configuration mr imaging system for radiation therapy planning and interventional MRI. International journal of computer assisted radiology and surgery. 2008;3(3):283-9.
20. Daanen V, Coste E, Sergent G, Godart F, Vasseur C, Rousseau J. Accurate localization of needle entry point in interventional MRI. J Magn Reson Imaging. 2000;12(4):645-9.
21. Tanner SF, Finnigan DJ, Khoo VS, Mayles P, Dearnaley DP, Leach MO. Radiotherapy planning of the pelvis using distortion corrected mr images: The removal of system distortions. Phys Med Biol. 2000;45(8):2117-32.
22. Doran SJ, Charles-Edwards L, Reinsberg SA, Leach MO. A complete distortion correction for mr images: I. Gradient warp correction. Phys Med Biol. 2005;50(7):1343-61.
23. Breeuwer MM, Holden M, Zylka W, editors. Detection and correction of geometric distortion in 3d mr images. Medical Imaging 2001; 2001: International Society for Optics and Photonics.
24. Commission IE. Iec tr 61948-1. Genova, Switzerland2001.
25. Baldwin LN, Wachowicz K, Fallone BG. A two-step scheme for distortion rectification of magnetic resonance images. Med Phys. 2009;36(9):3917-26.
26. Baldwin LN, Wachowicz K, Thomas SD, Rivest R, Fallone BG. Characterization, prediction, and correction of geometric distortion in 3 t mr images. Med Phys. 2007;34(2):388-99.
27. Http://modusmed.Com/grid3d-qa-phantom.
28. Besl P, McKay N. A method for registration of 3d shapes. IEEE Trans on Pattern Analysis and Machine Intelligence. 1992;14(2):239-56.